Research Article Vol. 12, No. 9 / September 2024 / Photonics Research 2033

PHOTONICS Research

Dynamic counterpropagating all-normal dispersion (DCANDi) fiber laser

Neeraj Prakash,[1] Jonathan Musgrave,[1] Bowen Li,[1,2,3] and Shu-Wei Huang[1,*]

[1]Department of Electrical, Computer, and Energy Engineering, University of Colorado Boulder, Boulder, Colorado 80309, USA
[2]Key Laboratory of Optical Fiber Sensing and Communications (Ministry of Education), University of Electronic Science and Technology of China, Chengdu 611731, China
[3]e-mail: bowen.li@uestc.edu.cn
*Corresponding author: ShuWei.Huang@colorado.edu

Received 29 April 2024; revised 3 July 2024; accepted 4 July 2024; posted 5 July 2024 (Doc. ID 528873); published 30 August 2024

The fiber single-cavity dual-comb laser (SCDCL) is an emerging light-source architecture that opens up the possibility for low-complexity dual-comb pump-probe measurements. However, the fundamental trade-off between measurement speed and time resolution remains a hurdle for the widespread use of fiber SCDCLs in dual-comb pump-probe measurements. In this paper, we break this fundamental trade-off by devising an all-optical dynamic repetition rate difference (Δf_{rep}) modulation technique. We demonstrate the dynamic Δf_{rep} modulation in a modified version of the recently developed counterpropagating all-normal dispersion (CANDi) fiber laser. We verify that our all-optical dynamic Δf_{rep} modulation technique does not introduce excessive relative timing jitter. In addition, the dynamic modulation mechanism is studied and validated both theoretically and experimentally. As a proof-of-principle experiment, we apply this so-called dynamic CANDi (DCANDi) fiber laser to measure the relaxation time of a semiconductor saturable absorber mirror, achieving a measurement speed and duty cycle enhancement factor of 143. DCANDi fiber laser is a promising light source for low-complexity, high-speed, high-sensitivity ultrafast dual-comb pump-probe measurements.

https://doi.org/10.1364/PRJ.528873

1. INTRODUCTION

Ultrafast pump-probe measurement has played a pivotal role in the study of femtosecond light–matter interaction and carrier dynamics as well as the characterization of chemical, solid-state, and biological materials [1]. Among all the variants, the dual-comb pump-probe technique offers a unique nonmechanical delay scanning mechanism that solves the measurement speed bottleneck and enables high-speed applications including terahertz time-domain spectroscopy [2–4], ultrafast photoacoustic characterization [5,6], high-sensitivity photothermal spectroscopy [7], multidimensional coherent spectroscopy [8,9], and coherent Raman spectroscopy [10–13]. In the dual-comb pump-probe technique, the delay scanning is controlled by setting the repetition rate difference (Δf_{rep}) between the two combs such that the two pulse trains will temporally walk off each other by steps of $\Delta f_{rep}/f_{rep}^2$, where f_{rep} is the average repetition rate. The total delay scan is $1/f_{rep}$, and the measurement speed is limited by $1/\Delta f_{rep}$.

The single-cavity dual-comb laser (SCDCL) is an emerging dual-comb architecture that has been studied over the past few years in various platforms including on-chip microresonators [14], Kerr-lens mode-locked lasers [15], semiconductor disk lasers [16], and fiber lasers [17–22]. Therein, fiber SCDCLs are a particularly attractive architecture owing to their compactness and environmental robustness. Fiber SCDCL opens up the possibility for low-complexity dual-comb systems and can potentially lead to a paradigm shift in dual-comb light-source development [23,24]. In particular, we recently demonstrated the counterpropagating all-normal dispersion (CANDi) fiber laser that pushed the energy limit in fiber SCDCLs by 2 orders of magnitude to 8-nJ pulse energy in each comb [25,26]. 190-fs compressed pulse duration and 39-fs integrated relative timing jitter (1 kHz, 20 MHz) have also been demonstrated and characterized. All these features render CANDi fiber laser an ideal source candidate for ultrafast dual-comb pump-probe measurements.

Another obstacle to the widespread adoption of the dual-comb pump-probe technique is the fundamental trade-off between the time resolution and measurement speed, due to their opposite scaling laws with respect to the Δf_{rep} [27]. In addition, for applications such as coherent Raman spectroscopy, where the vibrational coherence lifetime of most molecules is only a few picoseconds, the dual-comb pump-probe technique's typical >1-ns total delay scan is much longer than necessary, resulting in a <1% measurement duty cycle and a

significant waste of dual-comb power that effectively lowers the measurement sensitivity [12]. To break the fundamental trade-off and enhance the time and energy efficiency, a few elegant ways have been devised recently by nonmechanical cavity length control of one of the dual combs [11,13,28]. Impressive results such as orders-of-magnitude measurement speed enhancement without sacrificing resolution and sensitivity and near 100% duty cycle coherent Raman spectroscopy have been demonstrated [11,13]. However, none of these methods are compatible with the SCDCL architecture, let alone fiber SCDCL.

In this paper, we devise an all-optical dynamic Δf_{rep} modulation technique that is applicable to SCDCL to overcome the fundamental trade-off between time resolution and measurement speed. We demonstrate a dynamic CANDi (DCANDi) fiber laser architecture and illustrate a dynamic Δf_{rep} switching between $>+10$ Hz and <-10 Hz at kilohertz-level modulation frequency. We characterize the relative timing jitter of DCANDi fiber laser to be the same as that of CANDi fiber laser, confirming that our all-optical dynamic Δf_{rep} modulation technique does not introduce excessive noise. Furthermore, the dynamic modulation mechanism is studied and validated both theoretically and experimentally. As a proof-of-principle experiment, we apply DCANDi fiber laser to measure the relaxation time of a semiconductor saturable absorber mirror (SESAM), achieving a measurement speed and duty cycle enhancement of 143 times compared to traditional dual-comb pump-probe measurement. DCANDi fiber laser is a promising light source for low-complexity, high-speed, high-sensitivity ultrafast dual-comb pump-probe measurements.

2. DCANDI: ARCHITECTURE AND PRINCIPLE

The simplified DCANDi laser configuration is shown in Fig. 1(a). The cavity of DCANDi laser is constructed similar to that in Ref. [25]. However, in order to bring Δf_{rep} closer to zero, the lengths of the passive fiber on the two sides of the ytterbium-doped fiber (YDF) are deliberately kept the same, which makes the cavity symmetric for both directions. The fiber section consists of ~2 m long 6-μm-core YDF (Thorlabs YB1200-6/125DC) and ~1 m of HI1060 passive fiber on each side of the YDF. The length of gain fiber is chosen to be long enough to achieve the gain asymmetry for dynamic modulation (mechanism discussed in Section 3 and Appendix A) but short enough to avoid reabsorption loss for efficient lasing. The mode locking is achieved using nonlinear polarization rotation. Moreover, the YDF is pumped bidirectionally by two 980-nm laser diodes with same power level to make the gain distribution inside the YDF symmetric for both directions. In this way, Δf_{rep} can be easily tuned to close to zero by fine-tuning the intracavity wave plates.

Under this condition, by modulating the current of either of the pumps (pump2 is modulated here) with a square waveform, the sign of Δf_{rep} can be dynamically flipped, as schematically shown in Fig. 1(b). In order to make sure the absolute value of Δf_{rep} is the same before and after flipping, a slow phase-locked loop (PLL) with 100 Hz control bandwidth is applied to pump1 to lock the average Δf_{rep} to zero. More details on the PLL can be found in Appendix E. Since the control bandwidth is much smaller than the modulation frequency (kilohertz), the PLL does not counteract the modulation. When the average value of Δf_{rep} is successfully locked to zero, the pulses from the two combs will temporally walk off each other alternatively as the sign of Δf_{rep} flips [Fig. 1(b)] without needing to walk off for a whole round trip. As a result, the temporal interferogram frequency (i.e., the DC detection frequency) will be twice the modulation frequency, instead of Δf_{rep}, as in a conventional DC system. In this way, the DCANDi system can dramatically increase its DC detection speed without sacrificing its temporal sampling resolution and pulse energy, thus providing an ideal tool for high-speed nonlinear DC applications.

3. MECHANISM OF DYNAMIC MODULATION IN DCANDI

The mechanism of pump power change-induced dynamic Δf_{rep} modulation is mainly attributed to the nonidentical center frequency change coupled with intracavity group delay dispersion (β_2), which is identified here through numerical simulation. The dependence of f_{rep} on pump power has been extensively studied in Refs. [25,26]. The change in f_{rep} due to change in pump power can be due to several factors, including spectral shift (ω_Δ) coupled with β_2, change in root mean square spectral width coupled with third-order dispersion, gain, and self-steepening terms. In Ref. [26], we identified the ω_Δ term coupled with β_2 to be the main coupling mechanism, resulting in pump-power-induced f_{rep} and Δf_{rep} change in the CANDi laser. Considering only this term, the total

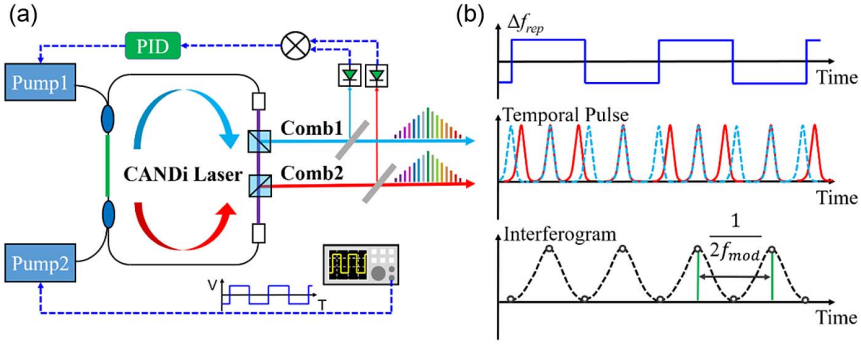

Fig. 1. Principle of operation. (a) Simplified experimental setup of the DCANDi laser; (b) (top) schematic diagram of the Δf_{rep} modulation; (middle) temporal walk-off of the two combs under modulation; (bottom) enhancement of interferogram repetition rate under modulation.

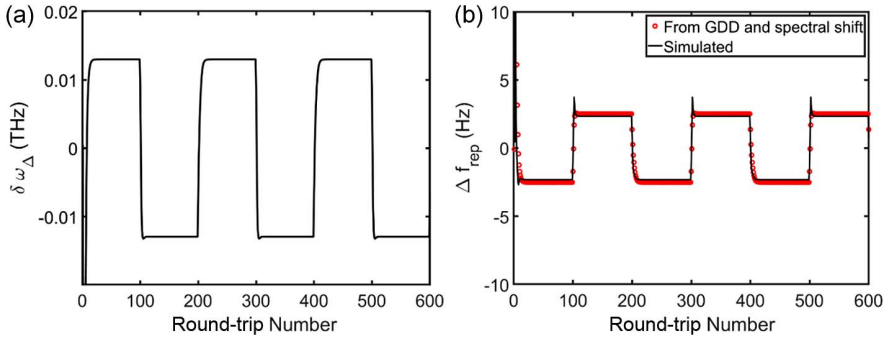

Fig. 2. DCANDi simulation routine results. (a) Modulation of the $\delta\omega_\Delta$ in DCANDi due to modulation of pump2 power; (b) comparison of the expected evolution of Δf_{rep} calculated from cavity β_2 coupled with ω_Δ (red circle) with the Δf_{rep} retrieved from pulse timing (black).

pump-power-(P)-induced changes in f_{rep} and Δf_{rep} are governed by the following equations, as explained in Ref. [26]:

$$\frac{\mathrm{d}f_{\text{rep}}}{\mathrm{d}P} = -f_{\text{rep}}^2 \times \left(\beta_2 \frac{\mathrm{d}\omega_\Delta}{\mathrm{d}P}\right), \tag{1}$$

$$\begin{aligned}\frac{\mathrm{d}\Delta f_{\text{rep}}}{\mathrm{d}P} &= -f_{\text{rep}}^2 \times \left(\beta_2 \frac{\mathrm{d}\omega_{\Delta_{\text{CW}}}}{\mathrm{d}P} - \beta_2 \frac{\mathrm{d}\omega_{\Delta_{\text{CCW}}}}{\mathrm{d}P}\right) \\ &= -f_{\text{rep}}^2 \times \left(\beta_2 \frac{\mathrm{d}\delta\omega_\Delta}{\mathrm{d}P}\right).\end{aligned} \tag{2}$$

In the above equation, $\omega_{\Delta_{\text{CW}}}$ and $\omega_{\Delta_{\text{CCW}}}$ are the spectral shift in clockwise (CW) and counterclockwise (CCW) directions, while $\delta\omega_\Delta$ is the relative spectral shift between the two directions. Since both combs in the DCANDi laser share the same pump, the mechanism for pump-power-induced change on Δf_{rep} can be attributed to the asymmetric response of the two directions to pump-power change. When only one of the pumps is modulated, the gain distribution along the length of the YDF becomes asymmetric for the two directions. This results in unequal gain center shift, resulting in different spectral shift for the two directions for a given pump-power change. This causes unequal change in f_{rep} in two directions and hence a change in Δf_{rep}.

To confirm this hypothesis, we developed a simulation routine to model DCANDi based on solving the generalized complex Ginzburg–Landau equation coupled with rate equations. Since the gain inside the YDF dynamically changes as the pump power is modulated, a key requirement of the simulation is to calculate the true gain by solving the rate equations and generalized complex Ginzburg–Landau equation simultaneously. Note that a steady state condition of upper state population and a perfect symmetric cavity is assumed in the simulation. The results of simulation are shown in the Figs. 2(a) and 2(b). Figure 2(a) illustrates the $\delta\omega_\Delta$ as a function of round trip for a particular mode-locked state as the pump power is modulated. Note that the simulation is displayed for 600 round trips, with the pump power modulated every 100 round trips. Figure 2(b) shows the comparison of the simulated Δf_{rep} deduced from the difference in pulse timing against Δf_{rep} calculated from the values in Fig. 2(a) using Eq. (2). The simulated Δf_{rep} matches well with the Δf_{rep} calculated using β_2 coupled with the $\delta\omega_\Delta$. This confirms that unequal gain center shift, resulting in different ω_Δ for the two directions for a given pump-power change is the main reason behind dynamic modulation of Δf_{rep}. More insights on the importance of longitudinal gain profile in causing pump-power-dependent $\delta\omega_\Delta$ can be found in the Appendix section. Later, in Section 4, we experimentally confirm the findings of the simulation to cement our understanding on the mechanism. More details on the simulation and simulation results are included in Appendix A.

These simulation results help us understand the mechanism of Δf_{rep} modulation in DCANDi laser and pave the way for custom designing DCANDis in the future. Beyond unraveling the mechanism of dynamic modulation in DCANDi, the simulation routine developed in this work contributes significantly to the broader field of SCDCL. The simulation can model complex interplay of parameters governing bidirectional SCDCL performance and help achieve precision controlled bidirectional SCDCL. The theoretical foundation discussed in this work can not only help optimize existing SCDCL designs but also lead to novel designs and applications.

4. RESULTS AND DISCUSSION

Figure 3 shows the basic performance of the DCANDi laser. Under static state (no current modulation), the optical spectra of the two combs are shown in Fig. 3(a). The two spectra show high spectral overlapping, and both represent a "batman" spectrum typical for ANDi lasers. The DCANDi laser has a repetition rate of 48 MHz and pulse energies of about 2 nJ for both directions. Higher pulse energies can be obtained by replacing the current 6-μm-core fibers with 10-μm-core large-mode area fibers [26]. A single-pulse compressor made of transmission grating pairs is used to compress pulses from both directions to around 180 fs, with total transmission of over 85% (see Appendix B for more details). Therefore, the peak power for compressed pulses is about 11 kW, which directly enables many nonlinear DC applications. To intuitively show the operation of dynamic Δf_{rep} modulation, we first modulate the current of pump2 with about 1 Hz frequency and simultaneously monitor the repetition rate of both combs using two frequency counters referenced to the same clock. The corresponding current modulation depth is around 3%, which does

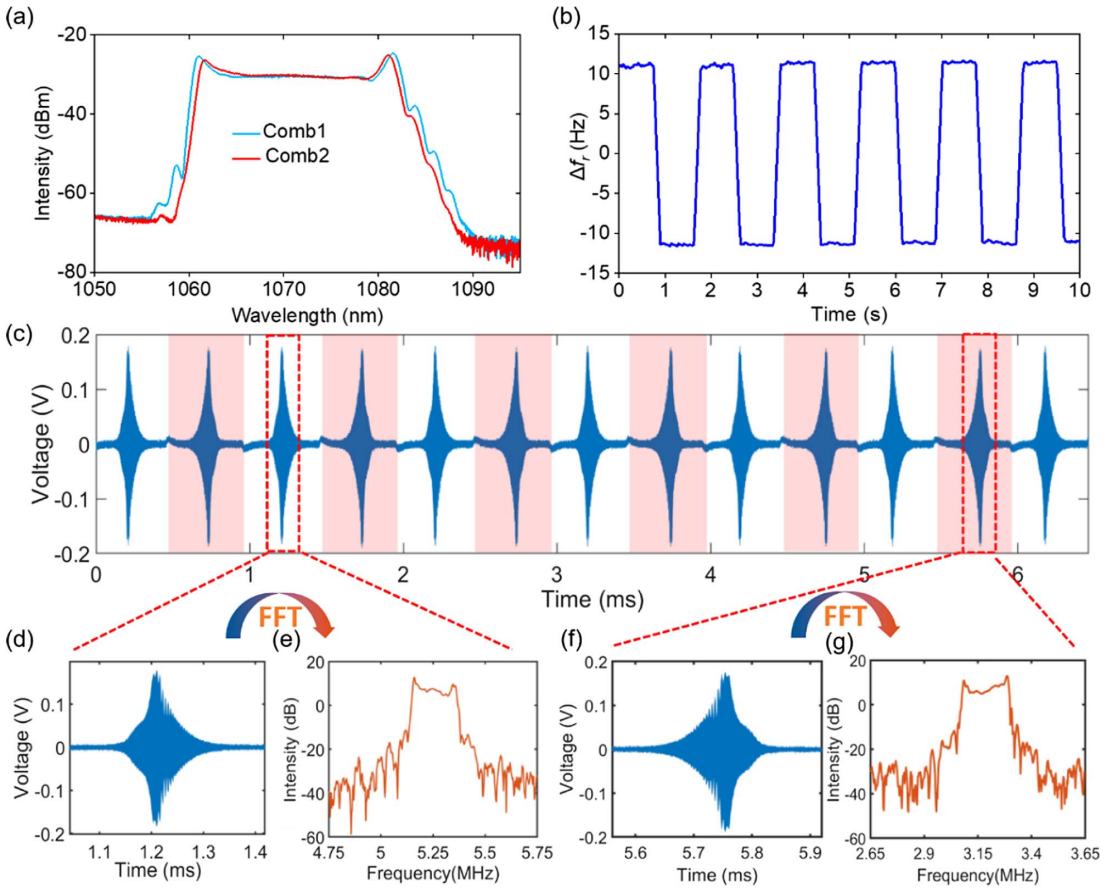

Fig. 3. Basic performance of DCANDi laser. (a) Optical spectra of the two combs without modulation; (b) evolution of repetition rate difference under slow pump modulation; (c) DC interferogram under 1 kHz modulation; interferogram during (d) forward and (f) backward temporal scanning; RF spectrum obtained from (e) forward and (g) backward interferogram.

not destroy the mode-locking state, thanks to the wide mode-locking range of ANDi lasers. The resulting Δf_{rep} is shown in Fig. 3(b), which periodically and deterministically switches from $\sim +11$ to ~ -11 Hz. The local fluctuation results from the limited resolution of frequency counter under 0.03 s arm time. To demonstrate the real potential of dynamic operation of the DCANDi laser, the modulation frequency is then increased to 1 kHz and the PLL is turned on. The two combs are then combined through a 50/50 coupler and launched together into an amplified photodetector. Since the pulses from the two combs do not walk off monotonically when the average Δf_{rep} is locked to zero, a variable optical delay line (ODL) is deployed on the path of one comb to make sure the pulses can temporally overlap each other at the PD. The output of the PD is low-pass filtered with 28 MHz; the corresponding temporal waveform is shown in Fig. 3(c). As expected, the temporal interferogram between the two combs shows a repeating frequency of 1 kHz, while two interferograms appear in each period, which results from forward and backward (shadowed with red) scanning. The time separations between a forward-scanning interferogram and two neighboring backward-scanning interferograms can be tuned to be identical by adjusting the relative delay between the two combs, leading to an effective DC detection speed of 2 kHz. The zoomed-in temporal waveforms of a forward-scanning and a backward-scanning interferograms are shown in Figs. 3(d) and 3(f), respectively, and their corresponding spectra are obtained by performing fast Fourier transform (FFT), as shown in Figs. 3(e) and 3(g). As observed, the two spectra are located at different center RF frequencies. This is due to the change of carrier-envelope-offset frequency (Δf_{ceo}) in response to the modulation of pump power. Nevertheless, both Figs. 3(e) and 3(g) show an RF spectrum that matches well with the overlapping optical spectrum in Fig. 3(a), which indicates the feasibility of fast and accurate DC metrology using the DCANDi laser.

In the previous section, using simulation, we identified the unequal ω_Δ in the two directions coupled with β_2 as the main reason behind the dependence of Δf_{rep} on pump power change. Here, we experimentally confirm this by measuring the evolution of the pulse spectrum in both directions during the pump-power modulation using the dispersive Fourier transform (DFT) technique. More information on measurement setup can be found in Appendix F. The modulation frequency was set at 5 kHz. The measured spectral evolution is shown in the appendix, while the $\delta\omega_\Delta$ calculated from the DFT measurements are shown in Fig. 4(a). Figure 4(b) shows the expected Δf_{rep} calculated based on Eq. (2) and data from Fig. 4(a). The β_2 coupled with $\delta\omega_\Delta$ results in Δf_{rep} change from ~ -11 to $\sim +11$ Hz. This matches with magnitude

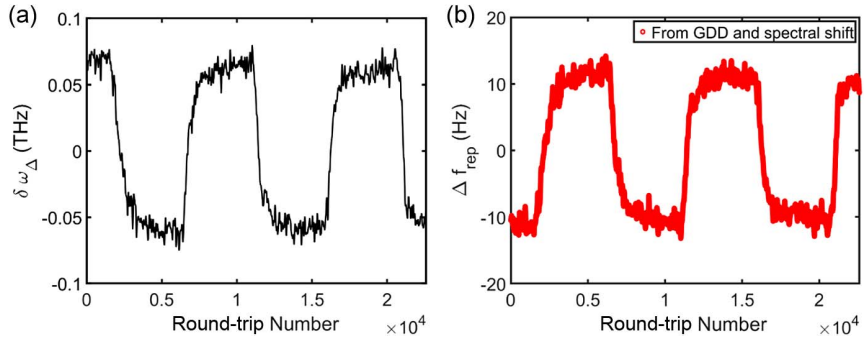

Fig. 4. (a) Evolution of the $\delta\omega_\Delta$ in DCANDi calculated from the spectral evolution measured using DFT; (b) evolution of Δf_{rep} due to the β_2 coupled with $\delta\omega_\Delta$ calculated using Eq. (2).

of dynamic modulation in Δf_{rep} achieved experimentally, as shown in the frequency counter measurement in Fig. 3(b). This validates the results from simulation and confirms that the unequal ω_Δ change due to pump-power change contributes the most in dynamic modulation of Δf_{rep}.

It should be noted that the difference in the modulation depth of Δf_{rep} in simulation and experiments is due to the difference in the mode-locking state in the experiment and simulation and also due to the fact that the simulation assumes a perfectly symmetric cavity, while it could be slightly asymmetric in the real experiments due to human error. However, the fact that dynamic modulation can be achieved even in a perfectly symmetric cavity, as shown through simulation results, rules out the necessity of cavity asymmetry (asymmetry in passive fiber length) for creating unequal response of the two directions to pump power and strengthens our understanding of spectral shifting playing the major role in this process. Since the asymmetric gain distribution along the length of the YDF in the two directions is the primary cause for realizing the dynamic tunable DC presented in this study, such dynamic modulation can be achieved in any symmetric bidirectional SCDCL systems where such an imbalanced longitudinal gain in the gain medium can be achieved. This is another advantage of bidirectional geometry compared to dual-wavelength and dual-polarization SCDCL systems, along with lesser cross talk and overlapping spectra. Hence, this technique is widely applicable in bidirectional SCDCL geometries, such as soliton fiber DCs and free-space DCs, and is not limited to CANDi lasers.

5. NOISE CHARACTERIZATION OF DCANDI

To ensure the enhanced frame rate in DCANDi does not come at the expense of CANDi's timing stability, we use DFT-based spectral interferometry to measure the relative timing jitter during dynamic modulation with femtosecond resolution. Experimental details on the measurement technique can be found in the appendix and in Ref. [26]. The spectral interferogram formed by the two separation-evolving comb pulses is shown in Fig. 5(a). The two positions around 140 and 290 μs, where the fringe density drops to zero, correspond to the times when the two comb pulses meet each other during the forward and backward scanning. By performing an FFT on the spectral fringes in each round trip, the evolution of pulse separation is reconstructed, as shown in Fig. 5(b). Furthermore, the

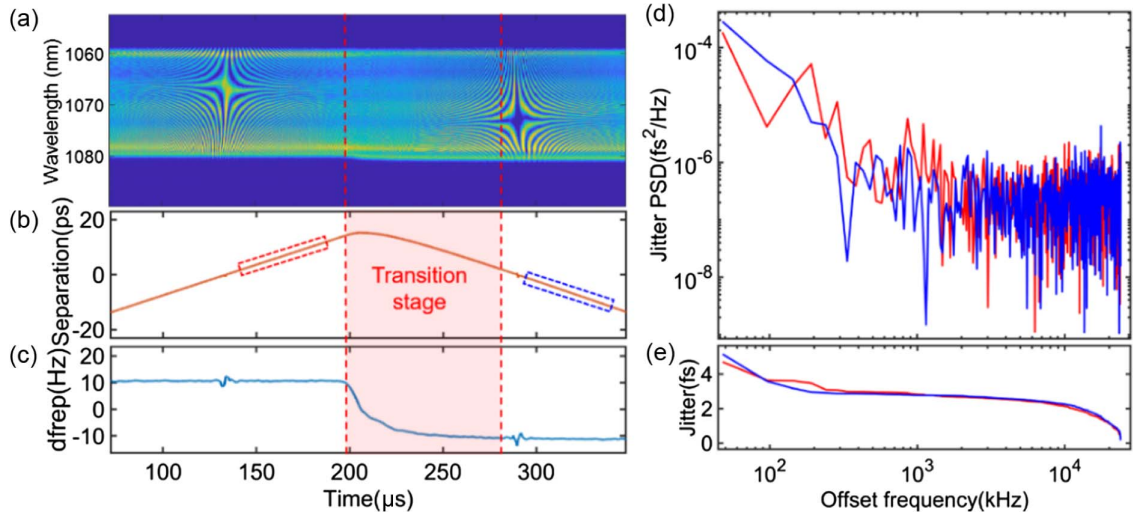

Fig. 5. Precise characterization of DC time-delay evolution during dynamic modulation. (a) Spectrogram during one Δf_{rep} switching; (b) pulse separation evolution obtained by performing FFT on (a); (c) Δf_{rep} evolution obtained from (b); (d) PSD of relative timing jitter calculated from 1000 consecutive round trips before (red) and after (blue) the transition, as marked in (b); (e) integrated timing jitter calculated from (d).

corresponding Δf_{rep} can be obtained by taking the derivative of separation evolution in neighboring round trips, as shown in Fig. 5(c). The local fluctuation at 140 and 290 μs was caused by the separation-retrieving error when the two pulses overlap with each other. The near-zero spectral fringe density makes the separation calculation inaccurate. Nevertheless, Figs. 5(b) and 5(c) clearly show the separation and Δf_{rep} evolution during the switching event. As observed, the two pulses first walk off with each other with constant speed before 195 μs. The corresponding Δf_{rep} was about 11 Hz. Then, the pump power dropped, which drove the Δf_{rep} to the negative value. The transition process took around 90 μs, after which the Δf_{rep} appeared stable at −11 Hz. The duration of transition process is attributed to the laser response bandwidth, which is around 10 kHz. This also sets the upper speed limit for the dynamic Δf_{rep} modulation. To verify the laser stability during dynamic operation, we calculate the relative timing jitter during 1000 consecutive round trips (48 μs) before and after the transition stage [marked by the red and blue dashed areas in Fig. 5(b)]. The corresponding power spectral densities (PSDs) and the corresponding integrated jitters are shown in Figs. 5(d) and 5(e), respectively. As observed, the PSDs for both time spans appear almost identical, and the integrated jitter (from 24 MHz to 20 kHz) is only around 5 fs, which is as stable as a conventional CANDi laser without modulation [26]. This result confidently proves that the dynamic modulation does not sacrifice the relative timing

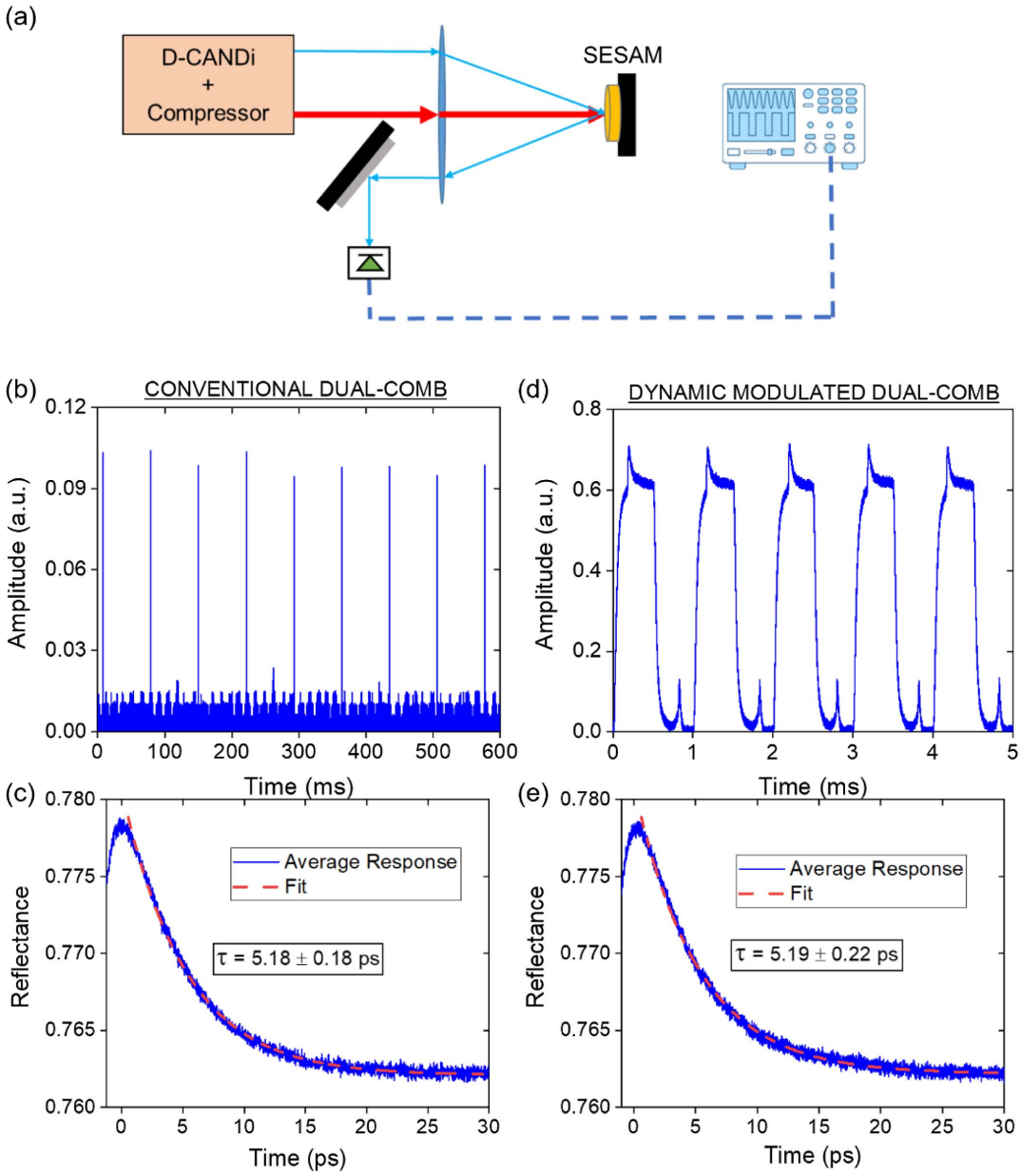

Fig. 6. Characterizing the relaxation time constant of SESAM. (a) Experimental setup. Pump-probe technique is employed in a reflection geometry. (b) Measured pump-probe signal using conventional DC technique for 600 ms; (c) mean response of the SESAM calculated by averaging nine pump-probe signals in (b); (d) measured pump-probe signal using proposed dynamic Δf_{rep} modulation technique for 5 ms; (e) mean response of the SESAM calculated by averaging nine pump-probe signals in (d).

stability, thus providing a powerful technique for significantly enhancing the DC detection speed using SCDCL.

6. FAST AND HIGH-FIDELITY NONLINEAR METROLOGY

To demonstrate the application of high frame rate and temporal resolution of the proposed dynamic Δf_{rep} modulation technique, we characterize the relaxation time constant of an off-the-shelf SESAM sample (from BATOP) using the DCANDi laser. The pump fluence incident on the SESAM is ∼58 μJ cm^{-2}, while the probe fluence is ∼0.5 μJ cm^{-2}. The pump-probe experiment was done in a reflection geometry, as shown in Fig. 6(a). The reflected probe was collected using a Si-switchable gain detector (Thorlabs PDA100A). The relaxation time constant is characterized in both conventional DC pump-probe and the dynamic Δf_{rep} modulation DC pump-probe methods. The results are shown in Figs. 6(b)–6(e). In the conventional DC method, where the Δf_{rep} was fixed at 14 Hz (temporal sampling time step is ∼6 fs), Fig. 6(b) shows the collected pump-probe signal for 600 ms (nine pump-probe curves) and Fig. 6(c) shows the averaged SESAM response, which reveals a time constant of 5.18 ± 0.18 ps. The same experiment was repeated using the dynamic modulation of Δf_{rep} at 1 kHz. Figure 6(d) shows the measured pump-probe signal using dynamic Δf_{rep} modulation technique for 5 ms. The temporal sampling time step is maintained at ∼6 fs. Figure 6(e) shows the average SESAM response, revealing a fitted time constant of 5.19 ± 0.22 ps. The number of pump-probe curves used for calculating the average response is kept at nine for both the techniques to ensure the same SNR.

Figure 6 confirms a frame rate enhancement of ∼143 (2000 Hz/14 Hz) without sacrificing resolution, sensitivity, and accuracy. Of note, while similar enhancement has been demonstrated in two-laser dual-comb systems [11,13], this is the first dynamic Δf_{rep} modulation demonstration using an SCDCL. The inherent common-mode-noise cancellation of SCDCLs helps in passively reducing relative timing jitter, which opens up the possibility for low-complexity dual-comb pump-probe measurements. Apart from frame rate enhancement, as a byproduct, assuming the noise is uncorrelated, one can also expect to obtain a higher SNR in the proposed dynamic Δf_{rep} modulation technique for same averaging time. From the standard deviation of the fitted response in both cases, it is also clear that dynamic modulation measurement has a similar error (or SNR) compared to the conventional case. Hence, the suggested technique can be used for employing higher frame rate or higher SNR depending on application.

7. CONCLUSION AND OUTLOOK

In summary, we demonstrate an all-optical technique to break the measurement speed-time resolution trade-off in SCDCL dual-comb pump-probe measurements. We achieve the all-optical dynamic Δf_{rep} modulation in a dual-pumped CANDi fiber laser by applying pump-power modulation to one of the pumps and showcase its basic operation. We present a simulation routine to accurately model the complex interplay of parameters governing bidirectional SCDCLs and use it to identify the unequal change in center frequency due to the asymmetric longitudinal gain distribution in the YDF as the mechanism of dynamic Δf_{rep} modulation of the DCANDi fiber laser. In addition, we confirm that the demonstrated all-optical dynamic Δf_{rep} modulation technique does not introduce excessive relative timing jitter and identify that the measurement speed is limited by the laser response bandwidth to 10 kHz. As a proof-of-principle experiment, we apply the DCANDi fiber laser to measure the relaxation time of an off-the-shelf SESAM and achieve a 143-fold enhancement in measurement speed and duty cycle. The DCANDi fiber laser is a promising light source for low-complexity, high-speed, high-sensitivity ultrafast DC pump-probe measurements. The working principle can be generalized to other SCDCL platforms where gain asymmetry in the two directions dominates the Δf_{rep}, thus representing a universal solution for breaking the measurement speed-time resolution trade-off in bidirectional SCDCLs. In particular, gain media with a shorter upper-state lifetime, such as highly doped Yb multicomponent glass [29], phosphate glass fiber [30], and Ti:sapphire crystal [31] can be utilized to further enhance the dynamic modulation speed above 10 kHz.

APPENDIX A: NUMERICAL SIMULATIONS

1. Simulation Routine

The numerical simulation for the DCANDi laser with gain dynamics is based on a model that jointly solves the rate equations (REs) and a coupled set of Ginzburg–Landau equations (CGLE), using a split-step Fourier method (SSFM). Limiting our model to include dispersion up to the third order and ignoring Raman effects, our set of coupled equations describing propagation takes the form

$$\frac{\delta U}{\delta z} = -\Delta\beta_1 \frac{\delta U}{\delta t} - i\frac{\beta_2}{2}\frac{\delta^2 U}{\delta t^2} - i\frac{\beta_3}{6}\frac{\delta^3 U}{\delta t^3} - \frac{\alpha - g}{2}U + i\gamma\left[\left(|U|^2 + \frac{2}{3}|V|^2\right) + \frac{1}{3}U^* V^2\right], \tag{A1.a}$$

$$\frac{\delta V}{\delta z} = -\Delta\beta_1 \frac{\delta V}{\delta t} - i\frac{\beta_2}{2}\frac{\delta^2 V}{\delta t^2} - i\frac{\beta_3}{6}\frac{\delta^3 V}{\delta t^3} - \frac{\alpha - g}{2}V + i\gamma\left[\left(|V|^2 + \frac{2}{3}|U|^2\right) + \frac{1}{3}V^* U^2\right]. \tag{A1.b}$$

U and V represent the electric fields in orthogonal polarizations, $\Delta\beta_1$ is the polarization mode dispersion, β_2 is the group velocity dispersion (GVD), and β_3 is the third-order dispersion (TOD). α is the intrinsic fiber loss. $\gamma = 2\pi n_2/\lambda A_{\text{eff}}$ is the nonlinear coefficient calculated using the effective mode area, A_{eff}, and the nonlinear index n_2. g represents the gain of the active fiber. For propagation through the segments of passive fiber, Eq. (A1) is sufficient to model the CW and CCW propagation directions. Without loss of generality, the following simulations ignored polarization dispersion as well as the intrinsic fiber loss ($\alpha = \Delta\beta = 0$).

To capture the gain dynamics in the active fiber, the frequency-dependent gain is calculated during the linear step of the SSFM using the pulse spectra and employing the

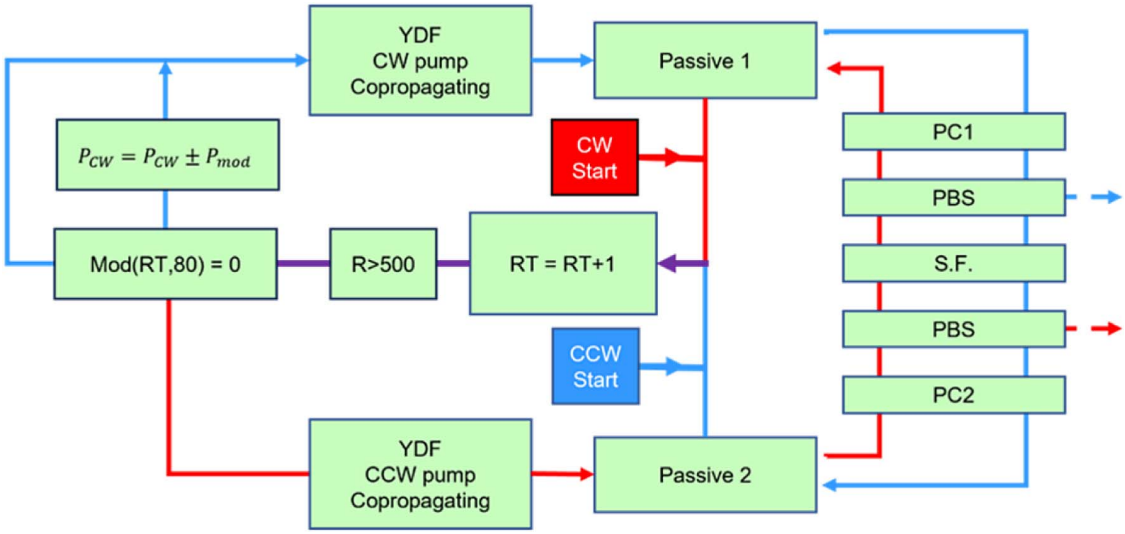

Fig. 7. Logic of the DCANDi simulation.

following set of REs valid for high repetition pulse amplification [32,33]:

$$\frac{\delta P_p}{\delta z} = \Gamma_p[\sigma_e N_2(z) - \sigma_a N_1(z)]\rho P_p, \tag{A2.a}$$

$$\frac{\delta P_s}{\delta z} = \Gamma_s[\sigma_e N_2(z) - \sigma_a N_1(z)]\rho P_s, \tag{A2.b}$$

$$N_2(z) = \frac{R_{12} + W_{12}}{R_{12} + R_{21} + W_{12} + W_{21} + \frac{1}{\tau_{21}}}. \tag{A2.c}$$

The spectroscopic data from Ref. [34] were used to calculate the emission (σ_e) and absorption (σ_a) cross sections. $\Gamma_{p(s)} = 1 - \exp(-2r_{\text{core}}^2/w^2)$ is the modal overlap of the signal, where r_{core} is the core radius and w is the mode field radius at $1/e^2$ approximated by the Whitely model [35]. The population inversion is calculated with R_{12} (W_{12}) and R_{21} (W_{21}) representing the stimulated absorption and emission rate for the pump (signal). For a fiber core-area A, $R_{ij} = \Gamma_p \sigma_{e,a} \cdot (P_p^+ + P_p^-)/\omega_p A$ and $W_{ij} = \Gamma_s \sigma_{e,a} P_s^{\pm}/\hbar\omega_s A$, where P_p^+ represents the copropagating pump and P_p^- is the counterpropagating pump, while $P_s^{\pm}$ represents signal power in CW and CCW directions. Finally, Eqs. (A1) and (A2) are coupled through the gain coefficient $\tilde{g} = \tilde{g}_0/[1 + (P_s^+ + P_s^-)/P_{\text{sat}}]$, where P_{sat} is the saturation power and $\tilde{g}_0$ is the small signal gain calculated at each step, δz, of the fiber using the following relation:

$$\tilde{g}_0 = \frac{1}{\delta z} \ln\left[\frac{P_s(z + \delta z)}{P_s(z)}\right]. \tag{A3}$$

The four wave plates in the cavity are modeled with two sets of polarization controllers (PCs). The transfer function of both PCs for the CW direction is represented as

$$T_{\text{PC}} = \begin{pmatrix} \cos\theta & -\sin\theta \\ \sin\theta & \cos\theta \end{pmatrix} \begin{pmatrix} e^{-i\phi/2} & 0 \\ 0 & e^{i\phi/2} \end{pmatrix} \cdot \begin{pmatrix} \cos\theta & \sin\theta \\ -\sin\theta & \cos\theta \end{pmatrix}. \tag{A4}$$

θ is the angle between the coordinates of the PC and the polarization beam splitter, and ϕ is the phase delay between the two orthogonal polarization components induced by the PC.

The logic of the simulation is illustrated in the flow chart in Fig. 7, and Table 1 shows the parameters and their values used in the simulation.

The full DCANDi simulation is based on two propagating frames of reference (FORs), one in which the slow time is in the FOR of the CW direction pulse and the other where the slow

Table 1. Parameters and Values Used in the Simulation

Table of Parameters			
Parameter	**Value**	**Units**	**Notes**
$\Delta\beta_1$	0	fs/mm	Polarization dispersion
β_2	22	fs^2/mm	GVD
β_3	30	fs^3/mm	TOD
n_2	2.19×10^{-20}	m^2/W	Nonlinear index
α	0	m^{-1}	Intrinsic fiber loss
NA_{core}	0.13	rad	Numerical aperture of core
NA_{clad}	0.2	rad	Numerical aperture of cladding
r_{core}	2.5	μm	Radius of core
r_{clad}	62.5	μm	Radius of cladding
τ_{21}	1.4	ms	Fluorescent lifetime
N_T	1.5×10^{26}	Atoms	Doping to match the specified Liekki absorption
λ_{p+}	976	nm	Pump wavelength
λ_{p-}	976	nm	Pump wavelength
ω_{center}	Calculated	THz	$\omega_{\text{center}} = \frac{\int_{-\infty}^{\infty} \omega S(\omega) d\omega}{\int_{-\infty}^{\infty} S(\omega) d\omega}$ where $S(\omega)$ is the optical spectrum
λ_{center}	Calculated	nm	$\lambda_{\text{center}} = \frac{2\pi c}{\omega_{\text{center}}}$ where c is the speed of light

time is in the FOR of the CCW direction. The CCW propagating signal experiences an inverse transfer function from the PC compared to the CW direction; thus the angles of the four wave plates of the DCANDi system can be represented by four variables, $\theta_1, \theta_2, \phi_1$, and ϕ_2.

The two counterpropagating pumpings of the DCANDi system require that each pass through the active fiber needs to be solved using a pair of propagation schemes: one from the end of the fiber into which the pulse is injected and propagated from the start ($z = 0$) to the end ($z = L$) of the fiber, and the other scheme where the direction is reversed. To solve the propagation from $z = L$ to $z = 0$, an iterative boundary value problem is solved by employing the shooting method, which solves the population inversion N_2 along the fiber. During propagation from $z = L$ to $z = 0$, the forward-propagating signal is not updated; rather, the previous propagation from $z = 0$ to $z = L$ is used to determine the population inversion, N_2, at each specific position along the fiber. The solution for the counterpropagating pump is updated, and the propagation is conducted from $z = 0$ to $z = L$ updating the forward signal and copropagating pump. This sequence is repeated until the solution converges within a specified tolerance.

The pumps copropagating with the direction 1 and direction 2 are referred to as the CW pump and CCW pump, respectively, and in propagating the CW and CCW signals through the active fiber, the iterative value problem is reversed. The pump power is modulated by changing the initial CW pump power after a given number of round trips, and thus simulates a square wave pump-power modulation. The nature of Eq. (A2) relies on the steady-state solution of the population inversion; thus, the system responds instantaneously to the power modulation. Therefore, this scheme does not capture the transient nature of the system into the different mode-locked states but rather translates the system instantaneously to the modulated mode-locked solution. We thus observe the switching dynamics on a time scale much faster than experimental observations (tens of round trips rather than millions). This allows us to simulate this system accurately while still conducting the numerical simulation on a commercial-grade computer.

2. Simulation Results

The mechanism of pump-power-induced change in Δf_{rep} was explored using the simulation routine for DCANDi. The simulation assumes a symmetric cavity structure with 2 m of YDF and 1 m of passive fiber (HI1060) on either side, forming the fiber system of the cavity.

Figures 8 and 9 show the evolution of the center wavelength inside the cavity along the propagation direction for

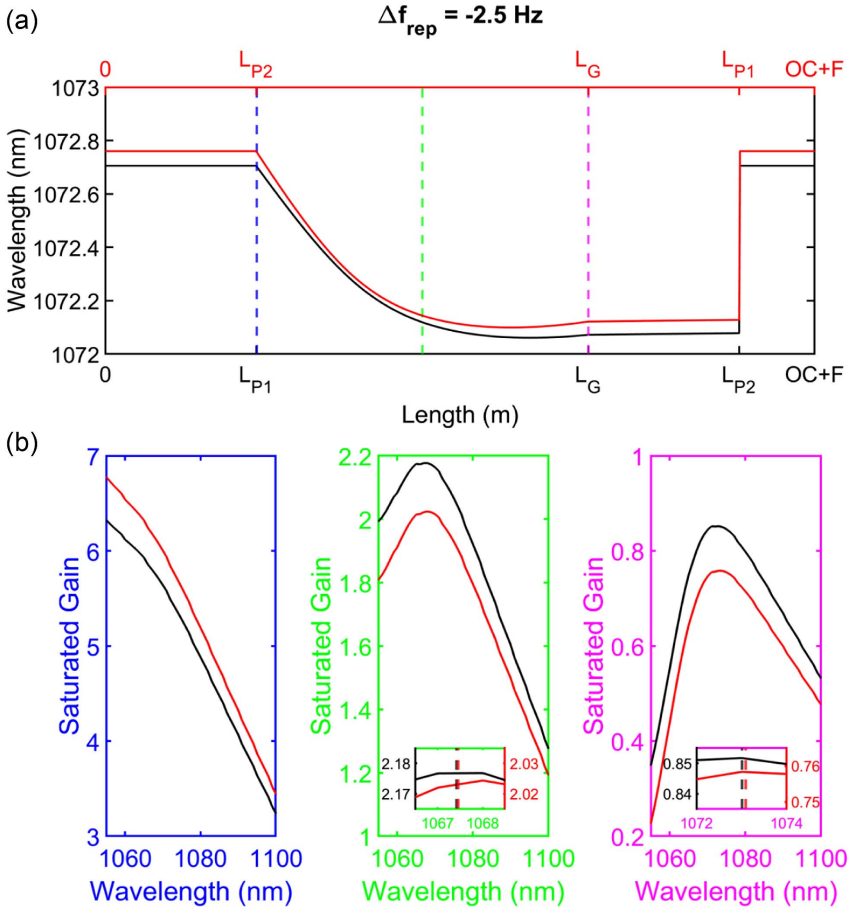

Fig. 8. (a) Evolution of center wavelength for direction 1 (black) and direction 2 (red) for the case of $\Delta f_{rep} = -2.5$ Hz; (b) comparison of the saturated gain spectrum of direction 1 (black) and direction 2 (red) at different points along the YDF marked in (a), which are the beginning, middle, and end of the YDF. The insets are zoomed-in to the gain peaks, and the dotted lines in the inset denote the center of the gain peak for each direction.

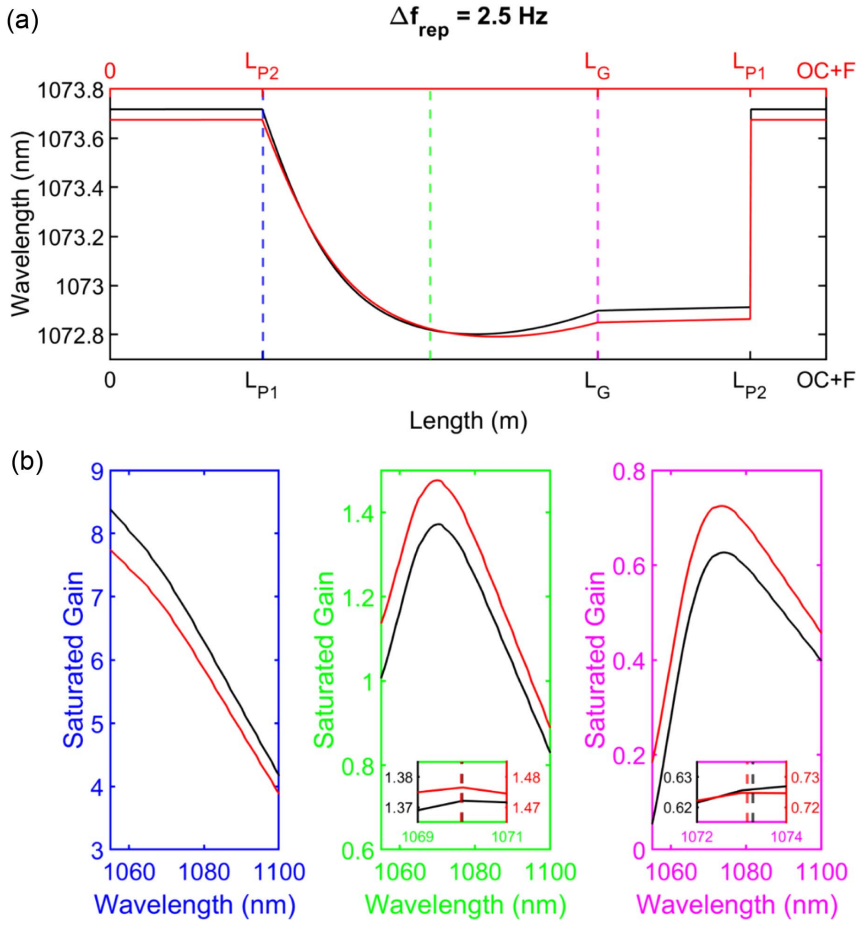

Fig. 9. (a) Evolution of center wavelength for direction 1 (black) and direction 2 (red) for the case of $\Delta f_{rep} = +2.5$ Hz; (b) comparison of the saturated gain spectrum of direction 1 (black) and direction 2 (red) at different points along the YDF marked in (a), which are the beginning, middle, and end of the YDF. The insets are zoomed-in to the gain peaks, and the dotted lines in the inset denote the center of the gain peak for each direction.

direction 1 (black curve) and direction 2 (red curve), along with the gain profile in three different points across the YDF. Figure 8(a) shows the evolution of the center wavelength for a negative Δf_{rep} (−2.5 Hz) situation. Note that the x axis for direction 2 is on the top of the graph. L_{P1} (or L_{P2}) denotes the end of the passive fiber 1 (or 2), and L_G denotes the end of the YDF. OC+F corresponds to the center wavelength of the spectrum after output coupling and filtering by the Gaussian filter in the cavity. Note that the x ticks for directions 1 and 2 are different, since the propagation direction inside the cavity for one is in the CW direction and the other is in the CCW direction. For this case, even though the difference between the center wavelengths in the two directions reduces in the beginning section of the YDF, the center wavelength of the direction 2 is always larger than that of direction 1. The evolution inside the YDF pushes the center wavelength of both the directions toward blue side, while the Gaussian filter readjusts it to a red wavelength. The saturated gain profiles of both directions at beginning (left, blue); middle (center, green); and end (right, magenta) of the YDF are shown in Fig. 8(b). For both directions, the gain is higher for shorter wavelength in the beginning part of the YDF due to the emission cross section of the YDF and gets reshaped as it propagates due to gain saturation pushing the gain peak to the red side, closer to the DCANDi spectral region. The gain saturation results in lesser gain in direction 2 with a redder gain peak [dotted lines in the insets of middle and right plots in Fig. 8(b)] compared to direction 1. The gain decreases for both directions, while the difference in gain peak center increases as it propagates along the YDF, with both gain peaks getting shifted to the red side.

Figure 9 shows the center wavelength evolution and gain curve for the case of positive Δf_{rep} (+2.5 Hz). Figure 9(a) shows the evolution of the center wavelength inside the cavity where the evolution behavior is different from Fig. 8(a). In this case, the center wavelength of direction 1 is larger than that of direction 2 both inside the passive fibers and after the Gaussian filter. However, within the YDF, although the center wavelengths of both directions are blueshifted in the initial length of the fiber, the center wavelengths have two crossing points where the center wavelength of direction 1 becomes smaller than that of direction 2 after the first crossing and becomes larger again once the center wavelengths start to redshift toward the back end of the YDF. The saturated gain profiles of both directions at beginning (left, blue); middle (center, green); and end (right, magenta) of YDF are shown in Fig. 9(b). Similar to the earlier case, for both directions, the gain peak is on the

shorter wavelength side in the beginning part of the YDF and gets pushed to the red side (closer to the DCANDi spectral region) due to gain saturation as the pulses are amplified inside the YDF. Even though the gain saturation results in lesser gain in direction 1 compared to direction 2, the peak gain wavelength [dotted lines in the insets of middle and right plots in Fig. 9(b)] for the two directions is almost similar at the middle of the YDF (closer to the second crossing). However, by the end of the YDF, the peak gain wavelength of direction 1 is redder compared to direction 2.

APPENDIX B: PULSE COMPRESSION

Both the combs from DCANDi are compressed using a common grating compressor in the transmission geometry. The grating compressor has a transmission of 85%. The compressed pulses are characterized using a conventional FROG setup; the results are shown in Fig. 10. The retrieved pulse duration, assuming a Gaussian pulse shape, of comb1 is about 171 fs, while that of comb2 is 185 fs. The slight difference in pulse duration could be attributed to the slight difference in spectral width and accumulated nonlinear phase along both directions. Note that the error in reconstructed spectrogram is less than 1% for both the cases.

APPENDIX C: DCANDI RESPONSE TO PUMP POWER

The dynamic modulation of Δf_{rep} in DCANDi is realized by modulation of one of the pump laser powers (pump2) while keeping the other pump power constant. Figure 11(a) shows the response of the Δf_{rep} to change in pump2 power. Note that the pump1 power is kept constant at 1.26 W, and measurement of Δf_{rep} is done using frequency counters. The response is almost linear, with a slope of ~0.2 Hz/mW and a tuning range of 34 Hz for a power change of 168 mW. These values depend on the mode-locking position, as different mode-locking positions can result in different slopes and tuning ranges. Note that, for the depicted mode-locking state, Δf_{rep} can be further increased by increasing the pump power up to 1.54 W without disturbing the mode locking. Above 1.54 W and below 1.26 W, the bidirectional mode-locking state is disturbed. Figure 11(b) shows the corresponding response of the output power in the two directions to the change in the pump2 power. Direction 2 (red) has smaller slope (0.036 mW/mW)

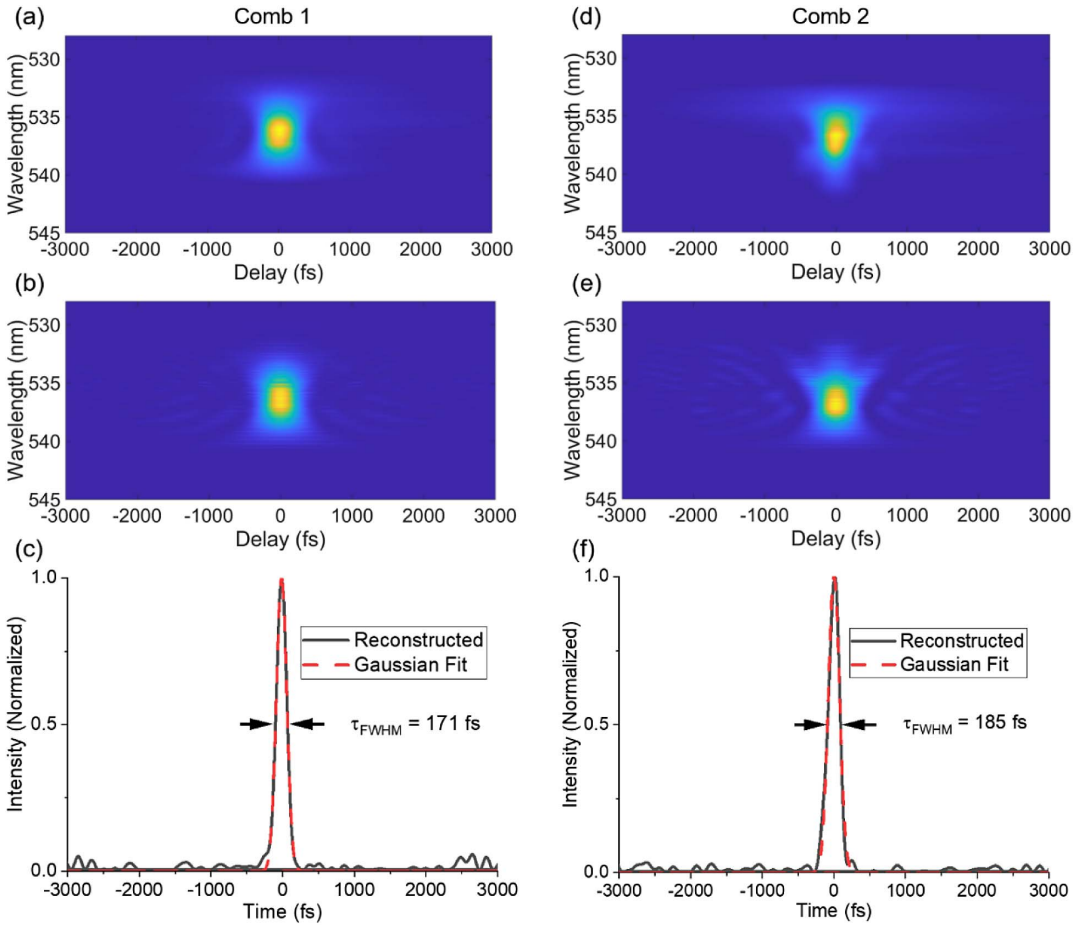

Fig. 10. Characterization of compressed pulse using a conventional FROG setup. In the figure, (a) and (b) are the measured and reconstructed spectrogram of comb 1, with (c) showing the retrieved pulse shape of comb 1. The Gaussian fitted pulse duration is 171 fs. Similarly, (d) and (e) are the measured and reconstructed spectrogram of comb 2, with (f) depicting the retrieved pulse shape of comb 2. The Gaussian fitted pulse duration is 185 fs.

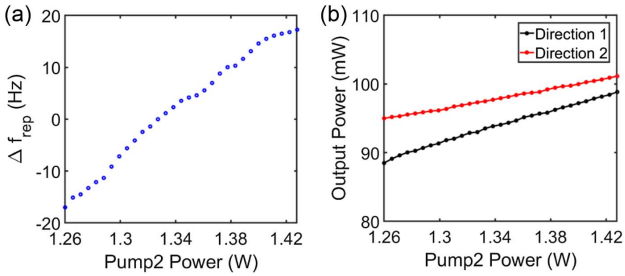

Fig. 11. (a) Response of Δf_{rep} to change in pump2 power. (b) Change in output power for direction 1 (black) and direction 2 (red) as a function of change in pump2 power. Note that the pump1 power is fixed at 1.26 W for this measurement.

compared to direction 1 (black) (0.062 mW/mW), with an overall change of 6.5% and 11.5% in output power for a change of 160 mW pump power. Note that these are the values for the whole tuning range. For a change of $\Delta f_{rep} = \pm 10$ Hz, the change in output power is lower (3.3% and 5.2%, respectively).

APPENDIX D: RESPONSE OF PUMP POWER TO SQUARE-WAVE MODULATION

Figure 12 shows the response of the pump power (measured using a photodiode) to square modulation that is applied to DCANDi for dynamic modulation of Δf_{rep}. Figures 12(a) and 12(b) show the response for 1 kHz modulation frequency and 5 kHz modulation frequency, respectively. The insets in both figures show a zoomed-in picture of the first rising edge of the square wave. In both cases, the modulation amplitude is kept constant at 250 mV. The response shows that the pump power follows the modulation wave well, at least until 5 kHz. However, the zoomed insets reveal that the pump power undergoes an oscillation relaxation-like behavior until ~50 μs before settling down. This implies that the maximum modulation frequency required to achieve a stable pump power is limited to <10 kHz (considering the full period of both high and low of the square wave). This implies a maximum pump-limited frame rate (or half-cycle) of 20 kHz in a DCANDi. However, as discussed in the main text, currently, the maximum frame rate of DCANDi is limited by the laser response to ~10 kHz.

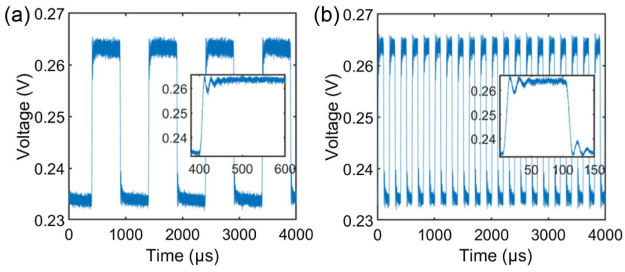

Fig. 12. Modulation of pump power by a square wave of (a) 1 kHz and (b) 5 kHz frequency. The insets show the zoomed-in picture of the first rising edge of the square wave. The amplitude of modulation is 250 mV.

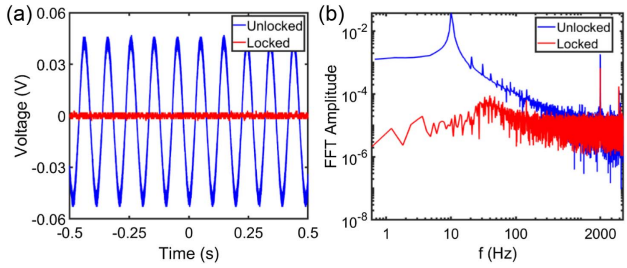

Fig. 13. (a) Error signal of the unlocked (blue) and locked (red) case measured with an oscilloscope; (b) FFT of the error signals in (a).

APPENDIX E: LOW-FREQUENCY PID LOOP

In order to make sure the absolute value of Δf_{rep} is the same before and after flipping, a slow PLL with 100 Hz control bandwidth is applied to pump1 to lock the average Δf_{rep} to zero. Since the control bandwidth is much smaller than the modulation frequency (a few kilohertz), the PLL does not counteract the modulation. To form the PLL, 1% of output power from both combs is fed into two photodetectors, respectively, to obtain the fundamental repetition frequency, which are then frequency-mixed. The output of the mixer serves as the error signal, which is seeded into a PID controller that generates the control signal for controlling the current of pump1. The PLL on the pump1 power is obtained by using only the proportional and integral options of the PID control in the Moku:Lab, with an overall gain of +21 dB, proportion gain of 12 dB, and integral gain of 50 dB. This results in a frequency bandwidth of ~100 Hz. Figure 13(a) shows the unlocked and locked error signal collected using an oscilloscope. With the locking, the slow frequency is suppressed and the standard deviation of error signal is reduced from 0.032 to 0.00006 V. The FFTs of the error signals are shown in Fig. 13(b). This shows that the noise until 100 Hz is well suppressed by the PLL, while the 2 kHz signal is not suppressed, implying that PLL does not affect the pump-power modulation operation.

APPENDIX F: DFT MEASUREMENT

The DFT measurement setup comprises a 10 km HI1060 fiber spool providing a group delay dispersion of 230 ps^2, followed by an ytterbium-doped fiber amplifier (YDFA) stage for amplification, a fast photodetector with bandwidth of 12.5 GHz, and a high-speed real-time oscilloscope (10 GHz). The net pulse energy launched into the setup is limited to ~25 pJ to avoid nonlinearity in the fiber. For measuring the evolution of the pulse spectrum in both directions during the pump power modulation, a pulse from each individual direction was sent to the DFT fiber spool alternatively while pump2 was modulated. For measuring the relative timing jitter of DCANDi, both directions are combined using a 50:50 coupler that has a polarization controller installed in one of the arms to align the polarization of the two pulses. One of the output arms of the 50:50 coupler is sent to the DFT fiber spool.

In order to experimentally validate the findings from simulation on the origin of dependence of Δf_{rep} on pump-power

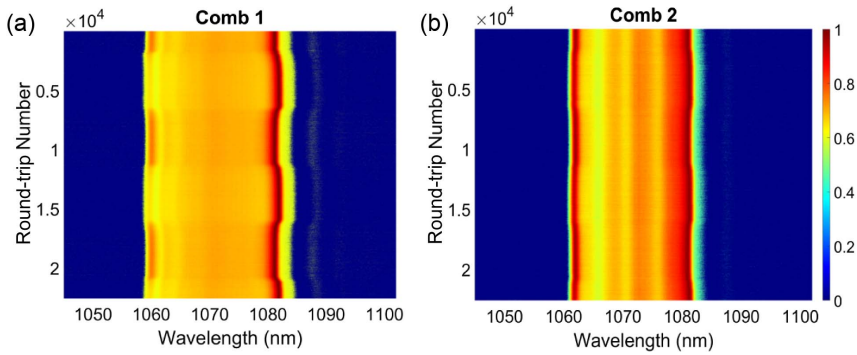

Fig. 14. Normalized spectral evolution along (a) direction 1 and (b) direction 2 while the pump2 is modulated, measured using the DFT technique.

change, we measured the evolution of the pulse spectrum in both directions during the pump-power modulation using the DFT technique. The spectral evolution of the two combs when pump2 power is modulated at 5 kHz frequency is shown in Figs. 14(a) and 14(b). Center wavelengths are calculated for each comb at each round trip, and these values are used in Eq. (2) in the main text to calculate the plots in Fig. 4(a) and subsequently Fig. 4(b). As observed, comb1 is more sensitive to pump-power change compared to comb2.

Funding. National Science Foundation (ECCS 2048202); Office of Naval Research (N00014-19-1-2251).

Acknowledgment. The authors acknowledge the Optics and Photonics Research Group at the University of Colorado Boulder supervised by Dr. Juliet Gopinath for providing the SESAM used in this work.

Disclosures. S.W.H. and B.L. are the inventors of the patent for CANDi fiber laser (US 11715926 B2). S.W.H., B.L., and N.P. are the inventors of the provisional patent application, filed by the University of Colorado Boulder, for the DCANDi fiber laser described in this paper.

Data Availability. Data underlying the results presented in this paper are not publicly available at this time but may be obtained from the authors upon reasonable request.

REFERENCES

1. A. M. Weiner, *Ultrafast Optics* (Wiley, 2011).
2. T. Yasui, R. Ichikawa, Y.-D. Hsieh, *et al.*, "Adaptive sampling dual terahertz comb spectroscopy using dual free-running femtosecond lasers," Sci. Rep. **5**, 10786 (2015).
3. G. Hu, T. Mizuguchi, R. Oe, *et al.*, "Dual terahertz comb spectroscopy with a single free-running fibre laser," Sci. Rep. **8**, 1–9 (2018).
4. R. D. Baker, N. T. Yardimci, Y.-H. Ou, *et al.*, "Self-triggered asynchronous optical sampling terahertz spectroscopy using a bidirectional mode-locked fiber laser," Sci. Rep. **8**, 14802 (2018).
5. J. Pupeikis, W. Hu, B. Willenberg, *et al.*, "Efficient pump-probe sampling with a single-cavity dual-comb laser: application in ultrafast photoacoustics," Photoacoustics **29**, 100439 (2023).
6. J. Pupeikis, B. Willenberg, F. Bruno, *et al.*, "Picosecond ultrasonics with a free-running dual-comb laser," Opt. Express **29**, 35735–35754 (2021).
7. Q. Wang, Z. Wang, H. Zhang, *et al.*, "Dual-comb photothermal spectroscopy," Nat. Commun. **13**, 2181 (2022).
8. B. Lomsadze, B. C. Smith, and S. T. Cundiff, "Tri-comb spectroscopy," Nat. Photonics **12**, 676–680 (2018).
9. B. Lomsadze and S. T. Cundiff, "Tri-comb multidimensional coherent spectroscopy," IEEE Photonics Technol. Lett. **31**, 1886–1889 (2019).
10. K. J. Mohler, B. J. Bohn, M. Yan, *et al.*, "Dual-comb coherent Raman spectroscopy with lasers of 1-GHz pulse repetition frequency," Opt. Lett. **42**, 318–321 (2017).
11. R. Kameyama, S. Takizawa, K. Hiramatsu, *et al.*, "Dual-comb coherent Raman spectroscopy with near 100% duty cycle," ACS Photonics **8**, 975–981 (2020).
12. T. Ideguchi, S. Holzner, B. Bernhardt, *et al.*, "Coherent Raman spectro-imaging with laser frequency combs," Nature **502**, 355–358 (2013).
13. Y. Zhang, M. Lu, T. Wu, *et al.*, "Delay-spectral focusing dual-comb coherent Raman spectroscopy for rapid detection in the high-wavenumber region," ACS Photonics **9**, 1385–1394 (2022).
14. Q.-F. Yang, X. Yi, K. Y. Yang, *et al.*, "Counter-propagating solitons in microresonators," Nat. Photonics **11**, 560–564 (2017).
15. T. Ideguchi, T. Nakamura, Y. Kobayashi, *et al.*, "Kerr-lens mode-locked bidirectional dual-comb ring laser for broadband dual-comb spectroscopy," Optica **3**, 748–753 (2016).
16. S. M. Link, D. Maas, D. Waldburger, *et al.*, "Dual-comb spectroscopy of water vapor with a free-running semiconductor disk laser," Science **356**, 1164–1168 (2017).
17. G. Hu, Y. Pan, X. Zhao, *et al.*, "Asynchronous and synchronous dual-wavelength pulse generation in a passively mode-locked fiber laser with a mode-locker," Opt. Lett. **42**, 4942–4945 (2017).
18. X. Zhao, T. Li, Y. Liu, *et al.*, "Polarization-multiplexed, dual-comb all-fiber mode-locked laser," Photonics Res. **6**, 853–857 (2018).
19. R. Li, H. Shi, H. Tian, *et al.*, "All-polarization-maintaining dual-wavelength mode-locked fiber laser based on Sagnac loop filter," Opt. Express **26**, 28302–28311 (2018).
20. K. Kieu and M. Mansuripur, "All-fiber bidirectional passively mode-locked ring laser," Opt. Lett. **33**, 64–66 (2008).
21. K. Zhao, H. Jia, P. Wang, *et al.*, "Free-running dual-comb fiber laser mode-locked by nonlinear multimode interference," Opt. Lett. **44**, 4323–4326 (2019).
22. Y. Nakajima, Y. Hata, and K. Minoshima, "High-coherence ultra-broadband bidirectional dual-comb fiber laser," Opt. Express **27**, 5931–5944 (2019).
23. C. Zhang, F. Qu, P. Ou, *et al.*, "Recent advances and outlook in single-cavity dual comb lasers," Photonics **10**, 221 (2023).
24. J. Yang, X. Zhao, L. Zhang, *et al.*, "Single-cavity dual-comb fiber lasers and their applications," Front. Phys. **10**, 1070284 (2023).
25. B. Li, J. Xing, D. Kwon, *et al.*, "Bidirectional mode-locked all-normal dispersion fiber laser," Optica **7**, 961–964 (2020).
26. N. Prakash, S.-W. Huang, and B. Li, "Relative timing jitter in a counter-propagating all-normal dispersion dual-comb fiber laser," Optica **9**, 717–723 (2022).

27. E. D. Caldwell, L. C. Sinclair, N. R. Newbury, *et al.*, "The time-programmable frequency comb and its use in quantum-limited ranging," Nature **610**, 667–673 (2022).
28. Y. Shi, D. Hu, R. Xue, *et al.*, "High speed time-of-flight displacement measurement based on dual-comb electronically controlled optical sampling," Opt. Express **30**, 8391–8398 (2022).
29. M. Loeser, F. Röser, A. Reichelt, *et al.*, "Broadband, diode pumped Yb: SiO_2 multicomponent glass laser," Opt. Lett. **37**, 4029–4031 (2012).
30. N. G. Boetti, D. Pugliese, E. Ceci-Ginistrelli, *et al.*, "Highly doped phosphate glass fibers for compact lasers and amplifiers: a review," Appl. Sci. **7**, 1295 (2017).
31. H. Jelínková, *Lasers for Medical Applications: Diagnostics, Therapy and Surgery* (Elsevier, 2013).
32. R. Lindberg, P. Zeil, M. Malmström, *et al.*, "Accurate modeling of high-repetition rate ultrashort pulse amplification in optical fibers," Sci. Rep. **6**, 34742 (2016).
33. H.-W. Chen, J. Lim, S.-W. Huang, *et al.*, "Optimization of femtosecond Yb-doped fiber amplifiers for high-quality pulse compression," Opt. Express **20**, 28672–28682 (2012).
34. R. Paschotta, J. Nilsson, A. C. Tropper, *et al.*, "Ytterbium-doped fiber amplifiers," IEEE J. Quantum Electron. **33**, 1049–1056 (1997).
35. T. J. Whitley and R. Wyatt, "Alternative Gaussian spot size polynomial for use with doped fiber amplifiers," IEEE Photonics Technol. Lett. **5**, 1325–1327 (1993).